LASER & PHOTONICS REVIEWS

www.lpr-journal.org

Smaller Stokes Shift Induced Highly Efficient Broadband Near Infrared Garnet Phosphor

Jingnan Zhang, Liangliang Zhang, Feng Liu, Hao Wu, Huajun Wu, Guohui Pan, Yongshi Luo, Zhendong Hao, and Jiahua Zhang**

Broadband near-infrared (NIR) phosphor converted light emitting diodes (pc-LEDs) are novel compact light sources that enable portable devices for substance detection. However, to achieve such efficient pc-LEDs is still a challenge due to lack of efficient phosphors. In this paper, Stokes shift as an efficiency predictor is emphasized. In Cr^{3+} activated $Ca_2LuZr_2Al_3O_{12}$ (CLZA) garnet phosphor, Stokes shift decreases from 2990 to 2854 cm^{-1} upon substituting Ca-Zr with Lu-Al. As a result, electron–phonon coupling related nonradiative process is reduced. The external quantum efficiency is significantly enhanced to 47.4%, and the as fabricated NIR pc-LED offers 33.7% @10 mA electro-optical efficiency. The results can advance the development of efficient NIR phosphors.

1. Introduction

Broadband near-infrared (NIR) phosphor converted light emitting diodes (pc-LEDs) based on blue LED chip are novel light sources that exhibiting attractive potential applications in substance noninvasive detection,[1,2] wearable devices for biosensing,[3,4] night vision,[5,6] and so on. To meet the demand of various applications, numerous studies have been conducted to develop efficient broadband NIR pc-LEDs.[4,7–11] In 2018, Shao and co-workers[12] reported $ScBO_3:Cr^{3+}$ NIR pc-LED with an emission band at 800 nm and the electro-optical efficiency of 7% at 120 mA drive current (7% @120 mA) or 12% @10 mA. In 2019, we fabricated $Ca_2LuHf_2Al_3O_{12}:Cr^{3+}$ NIR pc-LED[13] with an emission band at 790 nm and the electro-optical efficiency of 21.28% @10 mA. In 2020, Xu and co-workers[14] reported $LiInSi_2O_6:Cr^{3+}$ NIR pc-LED with an emission band at 840 nm and the electro-optical efficiency of 23% @10 mA. In 2021, Zhong and co-workers[15] achieved electro-optical efficiency of 26.6% @30 mA in $Ga_{2-x}In_xO_3:Cr^{3+}$ NIR pc-LED with an emission band at 713 nm. Very recently, we realized a high electro-optical efficiency of 30.6% @10 mA in $CaLu_2Mg_2Si_3O_{12}:Cr^{3+}$ garnet phosphor converted NIR pc-LED with an emission band at 750 nm.[16] For the NIR pc-LED with the emission band at 800 nm, the theoretical electro-optical efficiency can reach 40%. To further boost the electro-optical efficiency of NIR pc-LED, achieving highly efficient phosphor is essential.

Recently, we reported an excellent garnet phosphor of $Ca_2LuZr_2Al_3O_{12}:Cr^{3+}$ (CLZA:Cr^{3+}) with emission band at 790 nm.[13,17] The advantage of CLZA:Cr^{3+} is its much higher absorption (>50%) compared to most Cr^{3+} doped phosphors (< 30%). Nowadays, low absorption is a great drawback of Cr^{3+} doped NIR phosphors,[18] because it results in low external quantum efficiency (EQE) of phosphor and, thus, low efficiency of pc-LED device. Although many NIR phosphors show high internal quantum efficiency (IQE) even ~100%,[19,20] their EQE is still low (<30%) as the result of low absorption ability. For comparison, the IQE of CLZA:Cr^{3+} is only 69.1%, but the EQE is 31.5%. A further increase of IQE of CLZA:Cr^{3+} have the benefit of producing more efficient NIR pc-LED device.

Stokes shift, named after George Gabriel Stokes,[21] describes the phenomenon that the emission always occurs at longer wavelength (low energy) side compared with the excitation light. In 1973, G. Blasse[22] developed Stokes shift into predicting efficiency and thermal stability of phosphor, based on the configuration coordinates diagram. Stokes shift is found to determine the nonradiative process through the cross-point of the excited state and the ground state in the configuration coordinates diagram.[23] Thus, Large Stokes shift can quench luminescence totally, while small Stokes shift have the benefit of high luminescence efficiency and thermal stability. Nowadays, the influence of Stokes shift is underestimated, especially in Cr^{3+} doped phosphors where electron–phonon coupling is strong.

In this paper, we focused on smaller Stokes shift induced efficiency improvement in CLZA:Cr^{3+} phosphor. CLZA:Cr^{3+} is modified by substituting Ca-Zr with Lu-Al, resulting in composition of $Ca_{1.92-x}Lu_{1.08+x}Zr_{1.92-x}Cr_{0.08}Al_{3+x}O_{12}$ (CLZA:*x*Al).

J. Zhang, L. Zhang, H. Wu, H. Wu, G. Pan, Y. Luo, Z. Hao, J. Zhang
State Key Laboratory of Luminescence and Applications, Changchun Institute of Optics, Fine Mechanics and Physics
Chinese Academy of Sciences
3888 Eastern South Lake Road, Changchun 130033, China
E-mail: zhangliangliang@ciomp.ac.cn; zhangjh@ciomp.ac.cn

J. Zhang, J. Zhang
Center of Materials Science and Optoelectronics Engineering
University of Chinese Academy of Sciences
Beijing 100049, China

F. Liu
Key Laboratory for UV-Emitting Materials and Technology of Ministry of Education
Northeast Normal University
Changchun 130024, China

The ORCID identification number(s) for the author(s) of this article can be found under https://doi.org/10.1002/lpor.202200586

DOI: 10.1002/lpor.202200586

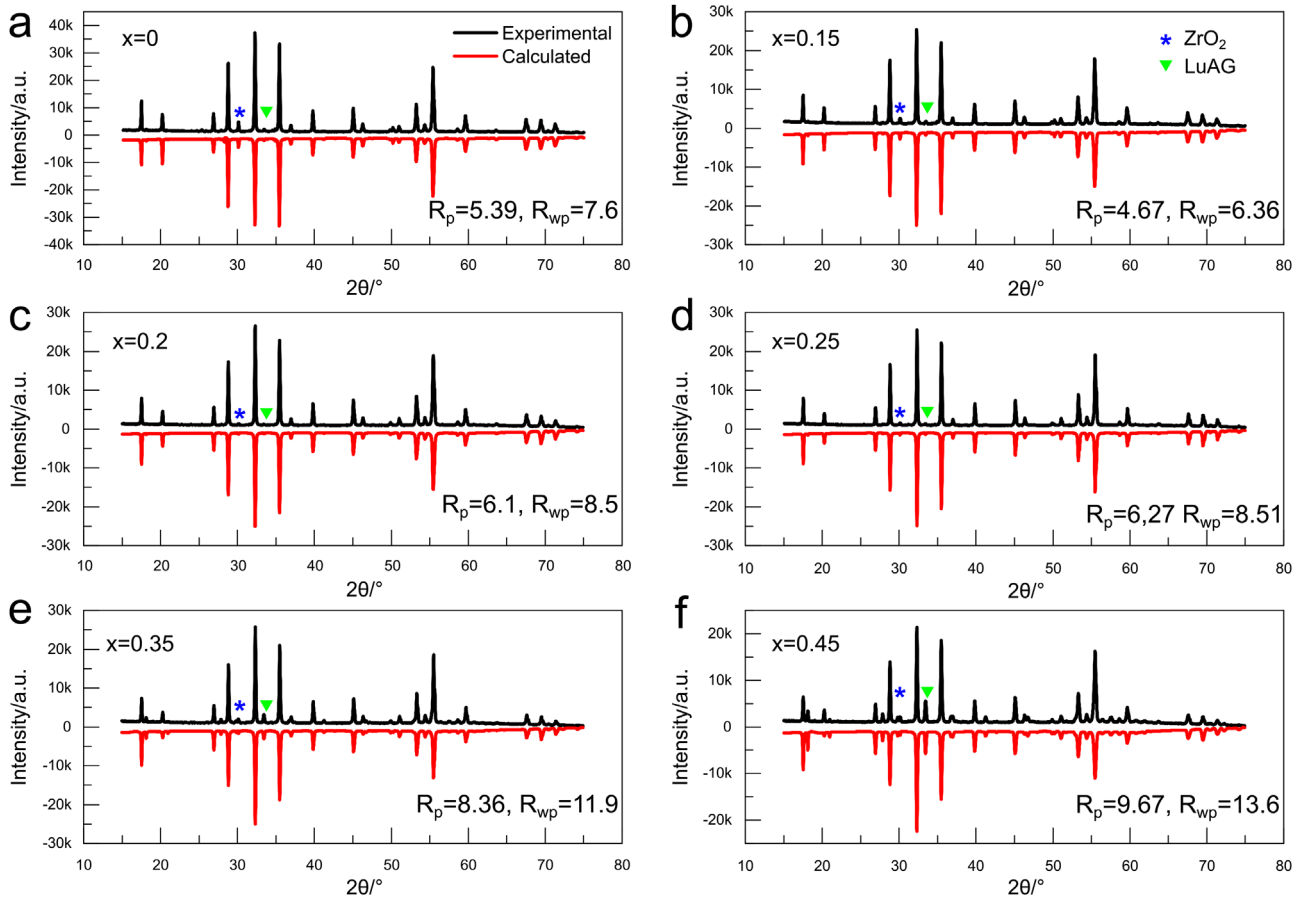

Figure 1. Rietveld refinement of XRD pattern. The blue symbol * represents the impurity ZrO_2 phase and the green symbol ▼ represents the impurity LuAG phase.

Photoluminescence (PL) properties of CLZA:*x*Al phosphors are studied as function of *x*. Meanwhile, markedly enhanced IQE of 84.8% and EQE of 47.4% are both achieved. The fabricated NIR pc-LED with an emission band at 790 nm offers a 33.7% @10 mA electro-optical efficiency, which is the highest efficiency among the broadband NIR pc-LEDs reported so far. The origin of the performance improvement of the CLZA:*x*Al phosphor is also studied by means of X-ray diffraction (XRD) patterns, PL, PL excitation (PLE), diffusion reflectance (DR) spectra, fluorescence decay curves. This paper aims to call for attention to Stokes shift for improving luminescence efficiency of broad band NIR phosphor.

2. Results and Discussion

Figure 1 shows the XRD patterns of $Ca_{1.92-x}Lu_{1.08+x}Zr_{1.92-x}Cr_{0.08}Al_{3+x}O_{12}$ ($x = 0, 0.15, 0.2, 0.25, 0.3, 0.4$) garnet phosphors. The black line is the measured experimental data and the red line is the calculated result by Rietveld method. The main XRD patterns well match $Ca_2LuZr_2Al_3O_{12}$ crystal structure in which Ca^{2+} and Lu^{3+} occupy the dodecahedral site, Zr^{4+} occupies the octahedral site, and Al^{3+} occupies the tetrahedral site. The radius of Ca^{2+}, Lu^{3+}, Zr^{4+}, Al^{3+} are 1.12 Å (CN = 8), 0.98 Å (CN = 8), 0.72 Å (CN = 6), and 0.39 Å (CN = 4), respectively. In $Ca_{1.92-x}Lu_{1.08+x}Zr_{1.92-x}Cr_{0.08}Al_{3+x}O_{12}$:0.08$Cr^{3+}$, Al^{3+} is designed to substitute for Zr^{4+} to occupy the octahedral site, while Lu^{3+} is designed to substitute for Ca^{2+} for charge balance. As Al^{3+} substitutes for Zr^{4+} in the octahedral site, the radius of Al^{3+} is 0.535Å (CN = 6). Because Al^{3+} is smaller than Zr^{4+} and Lu^{3+} is smaller than Ca^{2+}, the co-substitution of Ca-Zr with Lu-Al will reduce the lattice parameter. As shown in **Figure 2**a, cell parameter a, b, c decreases with increasing *x* value. However, the relationship between cell parameter and *x* deviates from linear regression. This signals the deviation of actual amount of ion substitution from the designed *x* value. When $x > 0.25$, the cell parameter even increases. This may be caused by rapid increase of ZrO_2 and $Lu_3Al_5O_{12}$ (LuAG) impurity phases. Zr^{4+} and Lu^{3+} may prefer to enter the two impurity phases.

As shown in Figure 1, two impurity phases, ZrO_2 and LuAG, are detected. The XRD peak of ZrO_2 is observed at 30.15° (marked by *), which is quite apparent for $x = 0$ (Figure 1a), indicating notable residue of ZrO_2 raw material. The Rietveld refinement shows that the amount of ZrO_2 phase decreases from 2.51 wt% to 0.39 wt% with x increasing from 0 to 0.2. Further increased *x* value results in more ZrO_2 impurity. The LuAG impurity peaks at 18.239°, 33.665°, and 41.543°. The amount of LuAG is ≈1 wt% when *x* is smaller then 0.25, and increases rapidly to 11.03 wt% when $x = 0.45$. Influence of ZrO_2 to luminescence of CLZA:*x*Al is slight because Cr^{3+} do not show luminescence in ZrO_2.

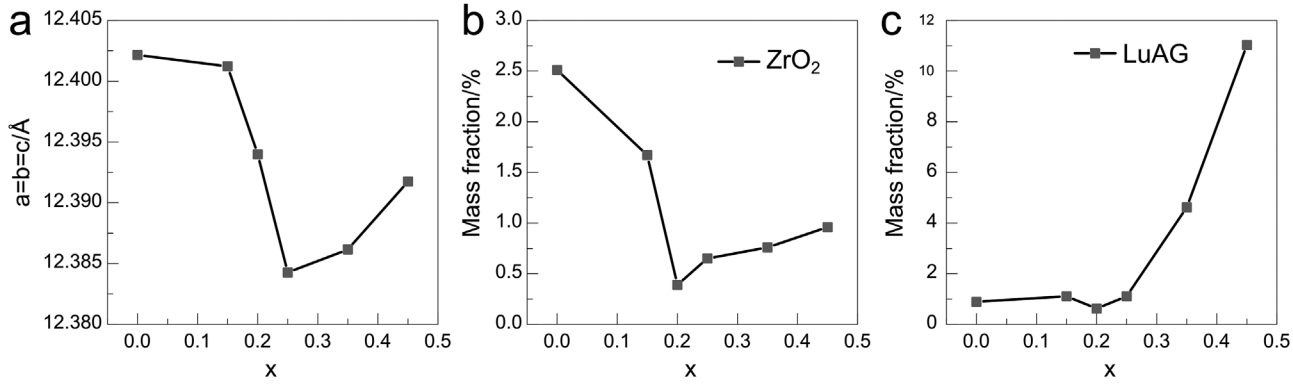

Figure 2. a) The cell parameter a, b, c of $Ca_{1.92-x}Lu_{1.08+x}Zr_{1.92-x}Cr_{0.08}Al_{3+x}O_{12}$. b) The mass fraction of ZrO_2 phase with different x value. c) The mass fraction of LuAG phase with different x value.

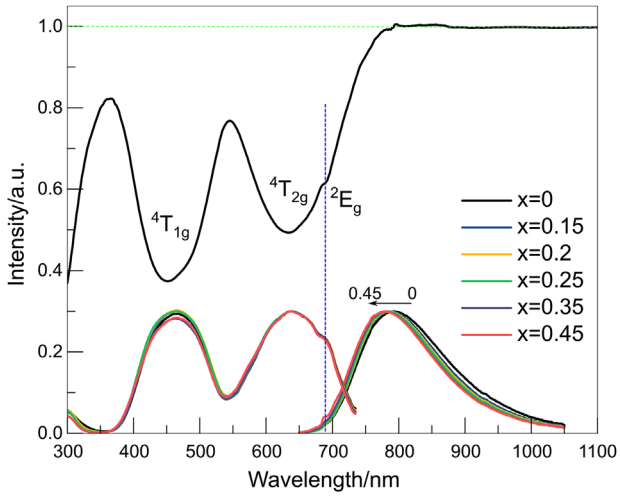

Figure 3. DR, PLE, and PL spectra of $Ca_{1.92-x}Lu_{1.08+x}Zr_{1.92-x}Cr_{0.08}Al_{3+x}O_{12}$.

However, influence of LuAG phase can be significant especially when x is larger than 0.35, because LuAG:Cr^{3+} shows a broad luminescence centers at ≈730 nm.[24] Overlap of emission spectra of LuAG:Cr^{3+} and CLZA:xAl is perceptible when $x = 0.35$ and $x = 0.45$. Overall, both ZrO_2 and LuAG impurities are lowest content, when $x = 0.2$.

The DR, PLE, and PL spectra of CLZA:xAl are shown in **Figure 3**. The DR and PLE spectra exhibit the well-known absorption transitions of Cr^{3+}, responsible for $^4A_{2g}$-$^4T_{1g}$ transition peaked at 450 nm and $^4A_{2g}$-$^4T_{2g}$ transition peaked at 650 nm. A sharp shoulder peak at 688 nm, originating from the transition between ^2E_g-$^4A_{2g}$, can be observed in DR, PLE, and PL spectra. The absorption of CLZA:xAl is as high as 63% suggested by the DR spectra, which is important for high EQE. The PL spectra shows a broad NIR band aroused from $^4T_{2g}$ -$^4A_{2g}$ transition of Cr^{3+}. The emission band exhibits a blueshift from 795 nm to 780 nm with x increasing from 0 to 0.45, as shown in Figure 3. However, the excitation peaks of $^4T_{2g}$ level are almost unchanged, resulting in smaller Stokes shift. Unchanged excitation peak may be caused by the opposite effect from crystal field and Stokes shift. Because Al^{3+} is smaller than Zr^{4+}, the crystal field is increased and the excitation peak position should show blueshift. However, the smaller Stokes shift has redshift effect on excitation peak because position of the excitation peak equals zero phonon line to subtract half of the Stokes shift. As the result, the peak position of excitation is almost unchanged. For the emission spectrum, both crystal field and Stokes shift have blueshift effect on emission position.

The emission intensity of CLZA:xAl increases with increasing x value and reaches maximum when $x = 0.25$, as shown in **Figure 4**a. The IQE and EQE of the phosphor at $x = 0.25$ is 84.8% and 47.4% excited by 450 nm. The absorption is 55.9%, which is similar to that measured by DR (63%) in Figure 3. One contributing factor to the increased emission intensity is the impurity amount. However, the content of impurities (both ZrO_2 and LuAG) is the lowest at $x = 0.2$, while the emission intensity is maximum at $x = 0.25$. This implies that the dominating factor did not arise from impurity. In this paper, we ascribe the dominant contributing to the smaller Stokes shift caused by Lu-Al substituting for Ca-Zr. Stokes shift related parameters all have minimum or maximum values at $x = 0.25$. As shown in Figure 4b, the emission peak position shows an obvious blueshift, while the excitation peak is almost unchanged. As a result, Stokes shift decreases from 2990 to 2854 cm^{-1} when $x = 0.25$. This indicates smaller electron–phonon coupling, and then a smaller bandwidth.[25] As shown in Figure 4c, FWHM also decreases from 2442 to 2301 cm^{-1} of $x = 0.25$. This result is in accordance with the changes in cell parameter that reaches minimum when $x = 0.25$, as shown in **Figure 2**a. Overall, with increasing x value, the highest solubility of Al^{3+} is reached at $x = 0.25$. Meantime, Stokes shift also decreases, reducing nonradiative process to increase emission efficiency. When $x > 0.25$, large amount of LuAG impurities quenches the emission intensity.

To understand the influence of Stokes shift on the x-dependent emission intensity, we have measured the decay curve of the emission after 450 nm pulse excitation, as shown in **Figure 5**a. It is apparent that the phosphors with $x = 0.25$ have a slower decay rate. The lifetime increases from 42 μs of $x = 0$ to 46 μs of $x = 0.25$. This result indicates suppressed nonradiative process with increasing x value. Smaller Stokes shift also results in better thermal stability of the phosphor. As shown in Figure 5b, the intensity at 420 K increases from 67.4% to 80.7% with x increasing from 0 to 0.25. An antithermal-quenching phenomenon

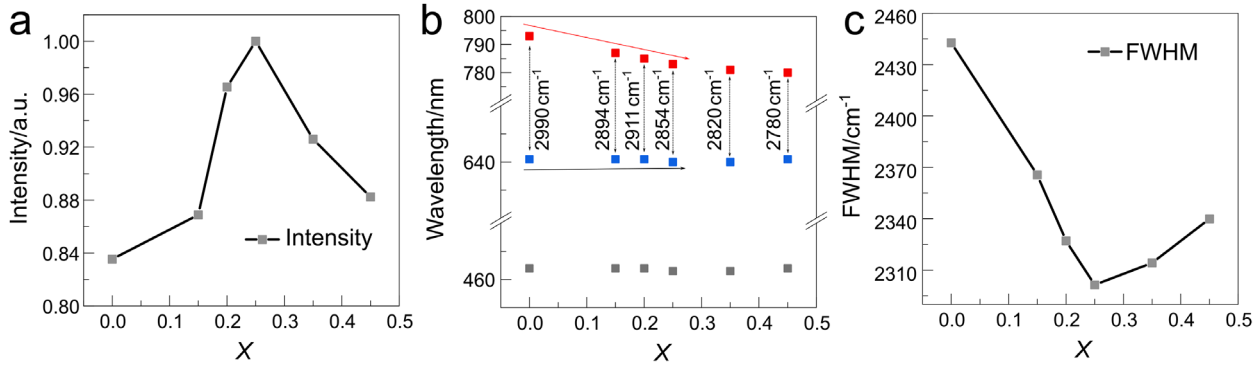

Figure 4. a) *x* dependence of NIR emission intensity of CLZA:*x*Al. b) Peak position of emission (red), excitation of $^4T_{2g}$ (blue), excitation of $^4T_{1g}$ (black) dependent on *x*. c) *x* dependence of bandwidth of CLZA:*x*Al.

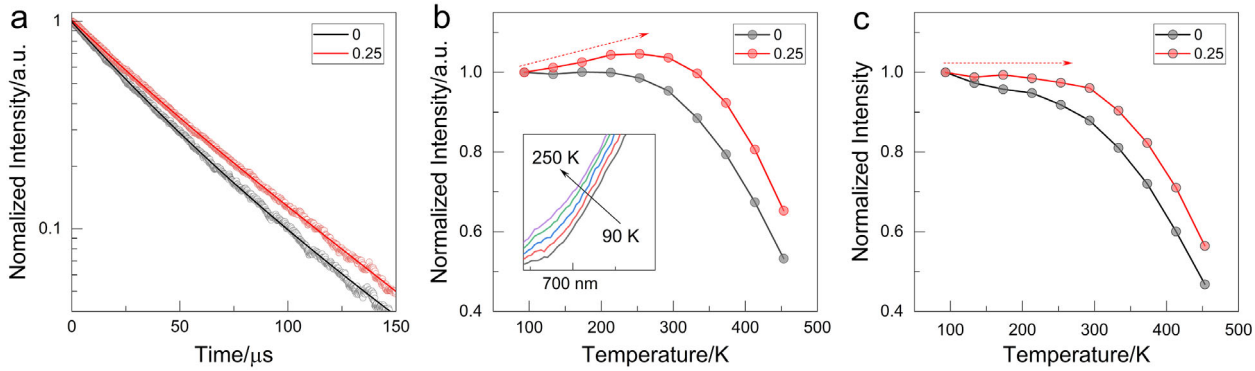

Figure 5. a) NIR fluorescence decay curve of CLZA and CLZA:0.25Al. b) Temperature dependence of emission integral-intensity of CLZA and CLZA:0.25Al. The insert figure is the emission spectra of CLZA:0.25Al around 700 nm at different temperature. c) Temperature dependence of emission peak-intensity of CLZA and CLZA:0.25Al.

is even observed in 90–250 K temperature range for $x = 0.25$. This result proves, again, increasing x value suppressed nonradiative process. The thermal-quenching phenomenon is examined by different intensity counting method. As shown in Figure 5c, the emission peak intensity of $x = 0.25$ is almost unchanged in 90–250 K temperature range. At the meantime, the emission band width increases at higher temperature for larger electron–phonon coupling. As shown in Figure 5b, the absolute intensity around 700 nm increases for stronger electron–phonon coupling in 90–250 K. As the result, the integral-intensity shows an antithermal-quenching phenomenon. As for $x = 0$, the emission peak intensity is decreased, while the emission bandwidth increases. As the result, the integral-intensity is almost unchanged. This result indicates that thermal quenching originated from electron–phonon coupling (Stokes shift) is smaller with increasing x value. Similar electron–phonon coupling induced antithermal-quenching phenomenon was also observed in Mn^{4+},[26,27] which has the same $3d^3$ electron configuration as Cr^{3+}. Overall, the decay curve and temperature dependent property prove that smaller Stokes shift reduces electron–phonon coupling related nonradiative process.

A broadband NIR pc-LED is fabricated by using a 450 nm LED chip and CLZA:0.25Al phosphor. The emission spectra of the pc-LED at various drive currents are shown in **Figure 6**a. The spectra show a NIR band peaking at 780 nm converted by the CLZA:0.25Al phosphor from the blue light at 450 nm of the LED chip. The blue band at 450 nm in the spectra is the transmitted light of the LED chip. The spectral intensity increases with the increase of drive current. The drive current dependences of NIR output power, electro-optical efficiency ($\eta_{pc\text{-}LED}$), and blue-to-NIR quantum conversion efficiency ($QE_{O\text{-}O}$)[14] are depicted in Figure 6b. The original data for the pc-LED are listed in Table S1 (Supporting Information) and the calculation of $\eta_{pc\text{-}LED}$ and $QE_{O\text{-}O}$ is performed using Equations (S1–S3), Supporting Information. The NIR output power can reach 73.3 mW at 100 mA drive current with the electro-optical efficiency of 24.4% @100 mA. At 10 mA drive current, the electro-optical efficiency can reach as high as 33.7%, which is the highest efficiency among the broadband NIR pc-LEDs reported so far, as shwon in **Table 1**.

CLZA:Cr^{3+} phosphor and the fabricated broadband NIR pc-LED can be applied for encryption. As shown in **Figure 7**a, the CLZA:Cr^{3+} phosphor with light green body color is mixed with a proper amount of ethyl alcohol to form a slurry as luminescent ink. Some numbers are handwritten by the ink on a piece of light green A4 paper. Under daily lighting sources, these handwritten numbers are invisible to the naked eye for the same color, as shown in Figure 7b. However, with a NIR camera, these handwritten numbers are visible because blue or red light from daily lighting sources can excite the CLZA:Cr^{3+} to luminescence, as shown in Figure 7b. Then, we try to illuminate the paper with

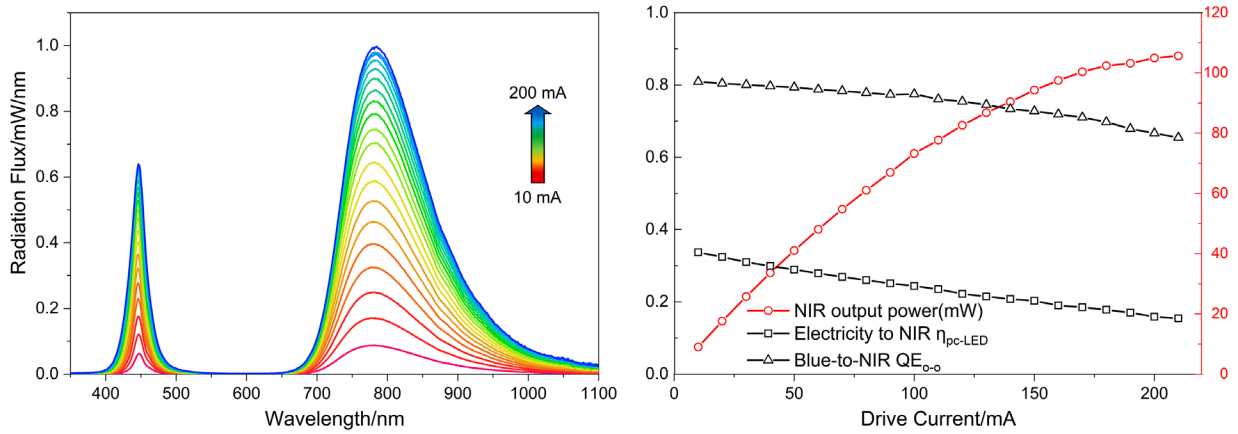

Figure 6. a) Emission spectra of CLZA:0.25Al NIR pc-LED under different drive currents from 10 to 200 mA. b) Drive current dependence of NIR output power, electro-optical efficiency ($\eta_{pc\text{-}LED}$), and blue-to-NIR quantum conversion efficiency ($QE_{O\text{-}O}$) of CLZA:0.25Al phosphor inside the NIR pc-LED.

Table 1. Peak wavelength of emission, IQE, EQE of typical broadband NIR phosphors and their NIR pc-LEDs with NIR output power and electro-optical efficiency ($\eta_{pc\text{-}LED}$).

Materials	λ_{em} [nm]	IQE [%]	EQE [%]	NIR output power@ Drive current	$\eta_{pc\text{-}LED}$	Refs.
$Ca_{2-x}Lu_{1+x}Zr_{2-x}Al_{3+x}O_{12}$: Cr^{3+}	780	84.8	47.4	9.0 mW @10 mA 73.3 mW @100 mA	33.9% @10 mA 24.4% @100 mA	This work
$CaLu_2Mg_2Si_3O_{12}$: Cr^{3+}	750	85.7	–	8.2 mW @10 mA 69.7 mW @100 mA	30.6% @10 mA 23.2% @100 mA	[14]
$Ga_{2-x}In_xO_3$: Cr^{3+}	713	88	–	21 mW @30 mA	26.6% @30 mA 17.2% @300 mA	[13]
$LiInSi_2O_6$: Cr^{3+}	840	75	–	51.6 mW @100 mA	23% @10 mA 17.8% @100 mA	[12]
$YAl_3(BO_3)_4$: Cr^{3+}	730	86.7	48.7	50.6 mW @100 mA	21.8% @10 mA 17.4% @100 mA	[28]
$Ca_2LuHf_2Al_3O_{12}$: Cr^{3+}	750	–	–	5.5 mW @10 mA 46.09 mW @100 mA	21.28% @10 mA 15.75% @100 mA	[11]

different extra light sources, as shown in Figure 7d. Figure 7g shows the photograph using the fabricated broadband NIR pc-LED in Figure 6 as an extra light source. We found these handwritten numbers are invisible again, even by the NIR camera. This is because the luminescent ink and the NIR pc-LED have the same spectra from CLZA:Cr^{3+}, as shown in Figure 7h. The light from NIR pc-LED covers the light from the luminescent ink. Then, we use a 785 nm NIR laser as an extra light source. These handwritten numbers are still visible by the NIR camera. This is because the spectra of CLZA:Cr^{3+} are broad and cannot be totally covered by the narrow band NIR laser, as shown in Figure 7e,f. Overall, spectra matching or mismatching between the luminesce ink and the extra light source provide multiple encryption modes.

3. Conclusion

Stokes shift is reduced in Cr^{3+} activated NIR $Ca_2LuZr_2Al_3O_{12}$ (CLZA) garnet phosphor through substitution of Ca-Zr with Lu-Al. The emission band exhibits a blueshift from 795 nm to 780 nm, while the excitation band is almost unchanged. This results in Stokes shift decreasing from 2990 cm^{-1} to 2854 cm^{-1}. As the result, the IQE is significantly enhanced to 84.8% at x = 0.25. Thanks to the good absorption ability of 55.9%, the EQE is increased to 47.4%. The lifetime increases from 42 μs of x = 0 to 46 μs of x = 0.25. An antithermal-quenching phenomenon in 90–250 K temperature range, which is not observed at x = 0, is observed at x = 0.25. These results indicate that a smaller Stokes shift reduces electron–phonon coupling related nonradiative process. The as-fabricated NIR pc-LED offers 33.7% @10 mA electro-optical efficiency, which is the highest efficiency among the broadband NIR pc-LEDs reported so far. The results proclaim that Stokes shift is a good predictor of electron–phonon coupling related nonradiative process that quenching luminescence. We call for more attention paid to Stokes shift for efficient Cr^{3+} doped NIR phosphors.

4. Experimental Section

Phosphor Synthesis: $Ca_{1.92-x}Lu_{1.08+x}Zr_{1.92-x}Cr_{0.08}Al_{3+x}O_{12}$ (x = 0–0.4) phosphors were prepared by the traditional high-temperature solid-phase method. The raw materials $CaCO_3$ (99.99%), Lu_2O_3 (99.9%), ZrO_2

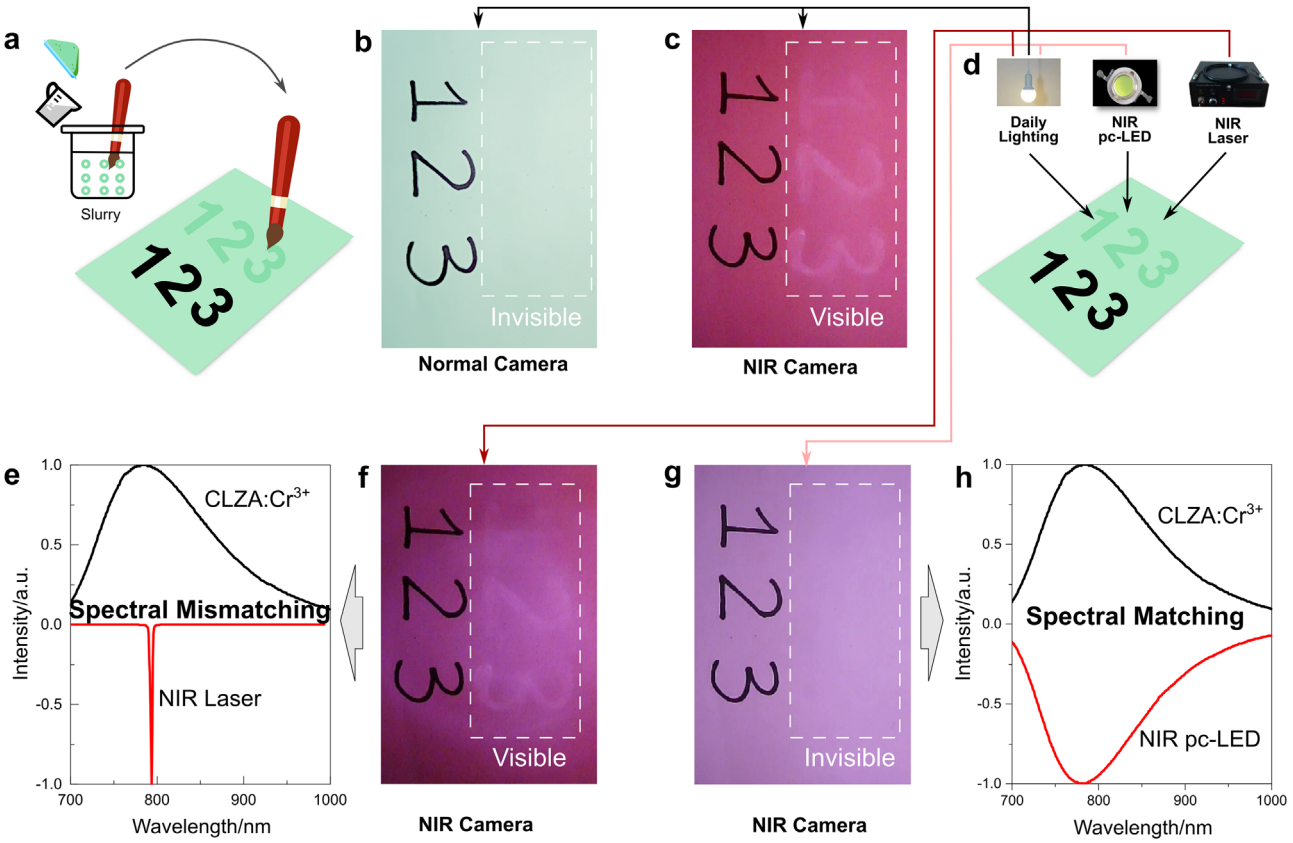

Figure 7. a) Fabrication of Luminescent ink and writing numbers on paper for encryption. b,c) Photograph taken under daily lighting conditions by normal camera and NIR camera, respectively. d) Diagram to show under different light sources. e) Spectra of CLZA:Cr^{3+} and NIR laser. f,g) Photographs taken by NIR camera under NIR laser and NIR pc-LED respectively. h) Spectra of CLZA:Cr^{3+} and NIR pc-LED.

(99.99%), Al_2O_3 (99.9%), Cr_2O_3 (99.99%) were weighed according to the stoichiometric ratio and were put into an agate mortar for fully grind. Then the well mixed mixture was transferred into a corundum crucible. Finally, the corundum crucible was put into a tube furnace for sintering. The sintering temperature is 1600 °C for 4 h with heating rate of 3 °C min^{-1}. The entire sintering process was carried out in a gas environment of 5% H_2 and 95% N_2.

Characterization and Measurements: XRD patterns were obtained on a D8 Focus diffractometer (Cu Ka, 40 kV, 40 mA, Bruker, Germany). The diffractometer was equipped with a LYNXEYE 1D detector to realize very quick measurement. The PL and PLE spectra were measured using an FL920 spectrometer (Edinburgh Instruments, UK) with a xenon lamp (Xe900) and a QEPro microfiber spectrometer (200–1000 nm, Ocean Optics, USA) equipped with a U-HGLGPS light source (Short arc mercury lamp, 130 W, Olympus, Japan). The IQE and EQE were measured using an absolute PL quantum yield measurement system (Quantaurus-QY Plus C13534-12, Hamamatsu Photonics). In the measurement of fluorescence decay, the 450 nm pulse laser with 10 ns duration of a Surelite II-10 pumped Horizon OPO was used as the excitation source, the signal was detected using an R9110 PMT TCSPC (Hamamatsu, Japan) and recorded by a TDS3052B Oscilloscope. Diffuse reflection (DR) spectra were measured by a UV-3600 plus spectrometer (Shimadzu, Japan). An integrating sphere system was equipped for powder DR measurement. $BaSO_4$ powder was used for calibration. A THMS600E cooling-heating platform (77–873 K, Linkam Scientific Instruments, UK) was used for offering different temperatures. The photoelectric properties of the pc-LEDs were measured using a HAAS 2000 photoelectric measuring system (350–1100 nm, EVERFINE, China).

Supporting Information

Supporting Information is available from the Wiley Online Library or from the author.

Acknowledgements

This work was financially supported by National Natural Science Foundation of China (Grant Nos. 12074373, 12074374, and 52072361), Key Research and Development Program of Jilin province (Grant No. 20210201024GX), Changchun science and technology planning project (Grant No. 21ZGY05), Youth Innovation Promotion Association CAS (No. 2020222), Opening Project of Key Laboratory of Transparent Opto-functional Inorganic Materials, Chinese Academy of Science.

Conflict of Interest

The authors declare no conflict of interest.

Data Availability Statement

The data that support the findings of this study are available from the corresponding author upon reasonable request.

Keywords

luminescence, NIR, pc-LED, phosphor, Stokes shift

Received: August 3, 2022
Revised: September 20, 2022
Published online:

[1] G. Zheng, W. Xiao, H. Wu, J. Wu, X. Liu, J. Qiu, *Laser Photonics Rev.* **2021**, *15*, 2100060.
[2] N. Ding, Y. Wu, W. Xu, J. Lyu, Y. Wang, L. Zi, L. Shao, R. Sun, N. Wang, S. Liu, D. Zhou, X. Bai, J. Zhou, H. Song, *Light: Sci. Appl.* **2022**, *11*, 91.
[3] V. K. Rajendran, P. Bakthavathsalam, P. L. Bergquist, A. Sunna, *Crit. Rev. Clin. Lab. Sci.* **2021**, *58*, 77.
[4] Y. Zhang, Q. Wei, Z. He, Y. Wang, T. Shan, Y. Fu, X. Guo, H. Zhong, *ACS Appl. Mater. Interfaces* **2022**, *14*, 31066.
[5] C. Yuan, R. Li, Y. Liu, L. Zhang, J. Zhang, G. Leniec, P. Sun, Z. Liu, Z. Luo, R. Dong, J. Jiang, *Laser Photonics Rev.* **2021**, *15*, 2100227.
[6] T. Zhu, L. Shen, D. Zhang, J. Zheng, X. Gong, *ACS Appl. Mater. Interfaces* **2022**, *14*, 18744.
[7] S. Miao, Y. Liang, Y. Zhang, D. Chen, X.-J. Wang, *ACS Appl. Mater. Interfaces* **2021**, *13*, 36011.
[8] H. Zhang, J. Zhong, F. Du, L. Chen, X. Zhang, Z. Mu, W. Zhao, *ACS Appl. Mater. Interfaces* **2022**, *14*, 11663.
[9] Y. Zhang, S. Miao, Y. Liang, C. Liang, D. Chen, X. Shan, K. Sun, X.-J. Wang, *Light: Sci. Appl.* **2022**, *11*, 136.
[10] S. Jin, R. Li, H. Huang, N. Jiang, J. Lin, S. Wang, Y. Zheng, X. Chen, D. Chen, *Light: Sci. Appl.* **2022**, *11*, 52.
[11] H. Huang, R. Li, S. Jin, Z. Li, P. Huang, J. Hong, S. Du, W. Zheng, X. Chen, D. Chen, *ACS Appl. Mater. Interfaces* **2021**, *13*, 34561.
[12] Q. Shao, H. Ding, L. Yao, J. Xu, C. Liang, J. Jiang, *RSC Adv.* **2018**, *8*, 12035.
[13] L. Zhang, D. Wang, Z. Hao, X. Zhang, G.-h. Pan, H. Wu, J. Zhang, *Adv. Opt. Mater.* **2019**, *7*, 1900185.
[14] X. Xu, Q. Shao, L. Yao, Y. Dong, J. Jiang, *Chem. Eng. J.* **2020**, *383*, 123108.
[15] J. Zhong, Y. Zhuo, F. Du, H. Zhang, W. Zhao, J. Brgoch, *ACS Appl. Mater. Interfaces* **2021**, *13*, 31835.
[16] H. Xiao, J. Zhang, L. Zhang, H. Wu, H. Wu, G. Pan, F. Liu, J. Zhang, *Adv. Opt. Mater.* **2021**, *9*, 2101134.
[17] L. Zhang, S. Zhang, Z. Hao, X. Zhang, G.-h. Pan, Y. Luo, H. Wu, J. Zhang, *J. Mater. Chem. C* **2018**, *6*, 4967.
[18] M. U. Dumesso, W. Xiao, G. Zheng, E. T. Basore, M. Tang, X. Liu, J. Qiu, *Adv. Opt. Mater.* **2022**, *10*, 2200676.
[19] E. T. Basore, W. Xiao, X. Liu, J. Wu, J. Qiu, *Adv. Opt. Mater.* **2020**, *8*, 2000296.
[20] Z. Jia, C. Yuan, Y. Liu, X.-J. Wang, P. Sun, L. Wang, H. Jiang, J. Jiang, *Light: Sci. Appl.* **2020**, *9*, 86.
[21] G. G. Stokes, *Philos. Trans. R. Soc. London* **1852**, *142*, 463.
[22] G. Blasse, *J. Solid State Chem.* **1974**, *9*, 147.
[23] B. Malysa, A. Meijerink, T. Jüstel, *J. Lumin.* **2018**, *202*, 523.
[24] D. Hayashi, A. M. van Dongen, J. Boerekamp, S. Spoor, G. Lucassen, J. Schleipen, *Appl. Phys. Lett.* **2017**, *110*, 233701.
[25] A. P. Vink, A. Meijerink, *Spectrochim. Acta, Part A* **1998**, *54*, 1755.
[26] T. Senden, R. J. A. van Dijk-Moes, A. Meijerink, *Light: Sci. Appl.* **2018**, *7*, 8.
[27] S. Adachi, *ECS J. Solid State Sci. Technol.* **2021**, *10*, 026002.
[28] M. Shi, L. Yao, J. Xu, C. Liang, Y. Dong, Q. Shao, *J. Am. Ceram. Soc.* **2021**, *104*, 3279.